Journal of Hydrology 388 (2010) 464–479

Contents lists available at ScienceDirect

Journal of Hydrology

journal homepage: www.elsevier.com/locate/jhydrol

Variability of snow water equivalent and snow energetics across a large catchment subject to Mountain Pine Beetle infestation and rapid salvage logging

Dan Bewley *, Younes Alila, Andrés Varhola

Department of Forest Resources Management, University of British Columbia, Canada

ARTICLE INFO

Article history:
Received 13 November 2009
Received in revised form 22 April 2010
Accepted 15 May 2010

This manuscript was handled by K. Georgakakos, Editor-in-Chief, with the assistance of Günter Blöschl, Associate Editor

Keywords:
Snow
Mountain Pine Beetle
Forest hydrology
Distributed modelling
Catchment scale

SUMMARY

This study examines the effect on stand and catchment scale snow processes due to widespread forest disturbance by the Mountain Pine Beetle (MPB; *Dendroctonus ponderosae*) infestation, for the 1570 km^2 Baker Creek catchment in the B.C. interior where all healthy mature lodgepole pine (*Pinus contorta*) stands which dominated the catchment up until 2000 have since died or been salvage logged. Measurements in 2008 and 2009 indicate that this net canopy reduction has reduced peak snowpack and melt rate differences between remaining stands (including large clearcuts, younger regenerating stands and dead mature pine stands), relative to a healthy forest canopy with smaller clearcuts. The Distributed Hydrology Soil Vegetation Model (DHSVM) was calibrated and run at 200 m resolution across the catchment, and simulated snowmelt rates and snow-covered area compared relatively well to distributed satellite or ground-based measurements. Snowpack and ablation rates were 10–20% higher during the 2008 and 2009 winters than when running the model for the pre-MPB landscape in 2000 using the same input meteorological data, resulting in almost no difference in the snowcover period. A greater snowpack volume which enters the stream network faster inevitably has implications for streamflows, flood risks and water resources, and these are assessed during the next stage of this research project.

1. Introduction

A snowmelt-dominated catchment will increasingly act as a seasonal, natural flood-control mechanism when more spatially diverse combinations of elevation, slope-aspect and forest cover stagger the meltwater release over a period of several weeks or months (Hendrick et al., 1971). The risk of flooding and enhanced streamflows to society and the environment (e.g., stream morphology, water quality and fish habitat) may therefore be reaching a critical level in the Interior Plateau region of British Columbia, since small elevational and slope-aspect gradients due to the gentle rolling topography are now being superimposed on a retreating forest cover dominated by lodegpole pine (*Pinus contorta*), due to the infestation by Mountain Pine Beetle (MPB; *Dendroctonus ponderosae*) since the late-1990's. MPB causes forest cover loss both naturally, when tree death is followed typically by needle removal after 3–5 years (Mitchell and Preisler 1998) and tree blowdown after 15–20 years (Lewis and Hartley, 2006), and anthropogenically as part of subsequent salvage logging operations. Canopy removal has shown to increase ground snowcover accumulation (e.g., Winkler et al., 2005), melt rates (e.g., Boon, 2007), and reduce net evapotranspiration (Ladekarl et al., 2001); the combination of which is likely to explain the increased annual water yields, seasonal streamflows, and earlier peak flows observed from hydrograph data in other catchments with insect-related disturbances (e.g., Bethlahmy, 1975; Potts, 1984). Distributed catchment-scale data of these processes, however, remain lacking for this particular disturbance type. At a decadal timescale, the magnitude and timing of MPB hydrologic and related impacts for the B.C. Interior Plateau region may depend on whether forest managers intensify current rates of salvage logging for greater short-term economic gain, or retain more dead forest. Interannual variability will inevitably depend on the amount of precipitation (e.g. Love, 1955), but also the seasonal weather patterns that control the degree of synchronisation in spatial meltwater delivery and runoff patterns (e.g. Lundquist et al., 2004).

Physically-based, spatially-distributed forest hydrology models of sufficient complexity are able to represent the spatial and temporal interactions between topography, vegetation and meteorology, which control variations in the distributions of snow cover, soil moisture and ultimately streamflows. These models, such as the Distributed Hydrology Soil Vegetation Model (DHSVM), provide a sophisticated method to examine land use disturbances on catchment hydrology, including conventional logging (e.g., Bowling et al., 2000), forest roads (LaMarche and Lettenmaier, 1998) and fire (Lanini et al., 2009). Similar attempts with insect infestation such as the current MPB outbreak are only at a preliminary stage, since stand-level results with which to initialise model

* Corresponding author. Present address: Hatfield Consultants, 200-850 Harbourside Drive, North Vancouver, BC, Canada V7P 0A3. Tel.: +1 778 230 3190.
E-mail address: dn_bewley@yahoo.co.uk (D. Bewley).

0022-1694/$ - see front matter © 2010 Elsevier B.V. All rights reserved.
doi:10.1016/j.jhydrol.2010.05.031

parameter values and verify simulated mass- and energy-balances have only become available since ~2006 (e.g., Teti and Winkler, 2008; Winkler and Boon, 2009; Boon, 2009). Additionally, the algorithms used within most forest hydrology models such as DHSVM may not be suited to MPB canopies which violate many of the underlying physical assumptions. For instance, in terms of snow processes, most canopy cover in dead stands (trunks, branches, snags etc.) is orientated vertically relative to a healthy stand with more randomly orientated foliage, such that scaling relationships optimised for the latter may fail (e.g., snowfall interception efficiency as a function of Plant Area Index; Koivusalo et al., 2006). Other processes, however, may be more easily adapted (e.g., subcanopy attenuation of short- and long-wave fluxes as a function of solar angle; Pomeroy et al., 2009). The effect on snow surface reflectance from unprecedented needle litter concentrations is unknown, and rapid salvage logging increases the potential of blowing snow processes in large clearcut areas; a process not simulated by forest hydrology models but which controls snow distribution in windy environments with short or no vegetation cover (e.g., Marks et al., 2002; Essery and Pomeroy, 2004).

This study aims to assess the spatial and temporal variability of Snow Water Equivalent across the Baker Creek catchment on the B.C. Interior Plateau, with small topographic diversity and extensive MPB-related disturbance. Stand-level measurements of SWE and various energy-balance components are used to calibrate the DHSVM model for improved simulation accuracy in representative MPB stands, and the model is run using fine-resolution (200 m) topographic and land cover data, and weather data interpolated from a network of eight automatic weather stations operating in 2008 and 2009. Simulated SWE values in individual stands and across the landscape are tested using ground-based and remotely-sensed data on snowcover properties. The snowpack variability across the current MPB landscape is then compared to the pre-MPB landscape with healthy forest cover, to determine the difference in snow accumulation and ablation rates at the catchment scale resulting from the MPB disturbance. Subsequent research will integrate the spatial and temporal snowmelt distributions resulting from this study within a transient, three-dimensional representation of surface and saturated subsurface flow (Wigmosta et al., 2002), in order to simulate the MPB effects on streamflow characteristics across the catchment. Collectively, these results will be of interest to forest and water resources managers when assessing the risk to infrastructure and other environmental variables, particularly for catchments like Baker Creek which lie towards the extreme end of topographic homogeneity and MPB-disturbance, and may therefore be of most hydrological concern.

2. DHSVM model

The original structure and equations forming the Distributed Hydrological Soil Vegetation Model (DHSVM) are described in full by Wigmosta et al. (2002), and for brevity only those processes controlling the ground snow cover accumulation and melt are summarised here.

2.1. Overview

The modelled landscape is divided into computational grid cells centered on Digital Elevation Model (DEM) data, with each cell or pixel assigned a set of parameter values describing the vegetation and soil characteristics. Vegetation may comprise of overstory vegetation (trees) which cover all or a prescribed fraction F of the pixel, whereas any understorey is assumed to cover the entire pixel. Meteorological conditions are prescribed at a specified reference height, including air temperature T_A, relative humidity RH, precipitation P, wind U and incoming short- and long-wave radiation ($K_\downarrow$ and $L_\downarrow$), of which only U, $K_\downarrow$ and $L_\downarrow$ are attenuated through the canopy. The DEM data in conjunction with specified lapse rates are used to adjust T_A and P topographically, with P partitioned into rainfall P_r and snowfall P_s using threshold values of T_A. Internal model calculations of pixel slope and azimuth angles are used to adjust $K_\downarrow$ but not $L_\downarrow$ to account explicitly for the topographic effects of slope and aspect. The model is then run hourly and generates one-dimensional energy and water balances for each pixel; aggregating these results for all pixels enables the distributions of spatial snow cover (and other hydrological variables such as soil moisture) to be determined. For clarity, common symbols used throughout the text are summarised in Table 1.

2.2. Ground snowpack model

Accumulation and melting of ground snowcover (i.e., under a canopy or in the open) is simulated using the two-layer coupled energy- and mass-balance model of Storck and Lettenmaier (1999) and Storck (2000), that explicitly accounts for the effects of topography and vegetation cover. The energy-balance components are used to simulate snowmelt, refreezing, and changes in the snowpack heat content, whereas the mass-balance components represent snow accumulation, ablation from melting or sublimation (but not wind redistribution), and water yield from the snowpack.

2.3. Canopy snow model

The canopy snow model also introduced by Storck and Lettenmaier (1999) and Storck (2000) is used to represent explicitly the combined canopy processes that govern snow interception, sublimation, mass release, and melt from the forest canopy. The change in intercepted snow amount (ΔI_s) in a certain time step t is simulated as a fixed percentage (interception efficiency I_e) of snowfall:

$$\Delta I_s = I_e \times P_s \quad (1)$$

until a maximum interception capacity (M) based on canopy density is reached:

Table 1
A list of commonly used stand, parameter and meteorological symbols used within the text, with description and units where applicable.

Code	Description	Units
CC	Clearcut stand (<7.5 year)	–
RN	Regenerating stand (7.5–15 year)	–
RG	Attacked juvenile stand (16–50 year)	–
GY	Mature dead pine stand (51+ year)	–
GN	Mature heathy pine stand (51+ year)	
Q_M	Melt energy flux (during melting)	W/m^2
Q_H	Sensible heat flux	W/m^2
Q_E	Latent heat flux	W/m^2
K_*	Net solar radiation	W/m^2
L_*	Net long-wave radiation	W/m^2
$K_\downarrow$	Incoming solar radiation	W/m^2
$L_\downarrow$	Incoming long-wave radiation	W/m^2
θ	Solar angle	°
τ_{pixel}	Pixel (stand) transmission coefficient	–
κ_{pixel}	Pixel (stand) extinction coefficient	–
I_e	Interception efficiency	–
PAI$_{pixel}$	Pixel (stand) PAI	m^2/m^2
F	Pixel vegetated cover	–
H	Canopy height	m
T_A	Air temperature	°C
Ts	Snow surface temperature	°C
P	Precipitation	mm
U	Wind speed	m/s
RH	Relative humidity	%
$SWE_{T/CC}$	SWE ratio (treed stand:clearcut)	–

$$I(t+\Delta t) = \min[I(t) + \Delta I, M] \quad (2)$$

Intercepted snow can be removed from the canopy through melt, sublimation, and mass release. Melting is calculated using an energy balance approach and results in drip (D). Mass release occurs if sufficient meltwater ($D_{\min}$) is generated during an individual time step such that the snow slides off the canopy, and is simulated as a fixed fraction (M/D ratio) of meltwater drip (Storck, 2000). Drip from the canopy is added to the ground snowpack as rain, while the cold content of any mass release or non-intercepted snow is accounted for in the ground snowpack energy balance.

2.4. Snowpack energy balance

The simulated change in temperature of the ground snowpack surface layer T_s over timestep Δt is calculated as:

$$T_s^{0+\Delta t} = T_s^0 + (\Delta t / c_s W)[K^* + L^* + Q_H + Q_L + Q_P + Q_M] \quad (3)$$

where T_s^0 is the initial snowpack temperature ($\leqslant 0$ °C), c_s is the specific heat of ice, W is the water equivalent of the snowpack, and the energy exchanges at the snow-air interface are: K^*, net shortwave (solar) energy; L^*, net longwave (thermal) energy; Q_H, sensible heat flux; Q_E, latent heat flux; Q_P, heat flux advected to the pack by rainfall, and Q_M is the energy flux given to the pack due to liquid water refreezing or taken from the pack during melt. Fluxes into the pack are taken as positive, and ground heat flux is neglected. If T_s remains below 0 °C over a time step, Q_M represents the gain of internal latent heat from refreezing of liquid water in the snowpack, but during melt when the pack is isothermal at 0 °C (i.e., $T_s^{0+\Delta t} = 0$) Q_M becomes the melt energy flux:

$$Q_M = K^* + L^* + Q_H + Q_L + Q_P \quad (4)$$

Q_H is proportional to the temperature gradient, and inversely proportional to the aerodynamic resistance r_{as}, between the snow surface and near-surface reference (measurement) height:

$$Q_H = \rho c_p (T_A - T_s)/r_{as} \quad (5)$$

where ρ is the density of air and c_p is the specific heat of air. r_{as} is adjusted for the effects of atmospheric stability and vegetation height H outlined by Storck (2000), but assumes that wind speed decreases exponentially through a specified crown height, and logarithmically above and below this point based on the work of Campbell (1977). Q_E is proportional to the vapour pressure gradient over the same height:

$$Q_E = \rho \lambda_i [0.622/P_a][e(T_A) - e_s(T_s)]/r_{as} \quad (6)$$

where λ_i is the latent heat of vaporisation when liquid water is present in the surface layer and the latent heat of sublimation in the absence of liquid water, P_a is atmospheric pressure, and e and e_s are the vapour pressures corresponding to T_A and T_S, respectively.

In the absence of an understory layer, the amount of shortwave radiation absorbed at the snow surface (K^*) is:

$$K^* = K\downarrow (1 - \alpha_s)\tau_{pixel} \quad (7)$$

where α_s is the value of snow albedo, and τ_{pixel} is the pixel-averaged fraction of $K_\downarrow$ transmitted through an overstory layer (i.e., vegetated pixel fraction $F > 0$). α_s is parameterised as a prognostic, exponential decay function of the snow age N (in days) which is reset to zero following fresh snowfall:

$$\alpha_S = \alpha_0 A^{N^{\wedge} B} \quad (8)$$

where α_0 is the albedo of fresh snow, and A and B are albedo decay coefficients which vary depending on whether the snow is under freezing or melt conditions, as determined by the snow surface temperature (T_s). τ_{pixel} is parameterised in the original version of DHSVM as proportional to F:

$$\tau_{pixel} = \tau_F F + [1 - F] \quad (9)$$

where τ_F, the fraction of solar energy transmitted through F, is calculated following a Beer's Law relationship of the form (Monteith and Unsworth, 1990):

$$\tau_F = \exp(-\kappa_F \mathrm{PAI}_F) \quad (10)$$

where κ_F is a constant extinction coefficient and PAI_F is the Plant Area Index, both representative of fraction F only. In effect, this scheme simulates vertical solar fluxes and neglects the shaded areas receiving only diffuse radiation which are cast across canopy gaps; this may therefore overestimate solar transmission particularly in MPB dead stands of low F value, which shade much of the snow surface especially during the snow-covered months when solar angles (θ) are lower. Based on the work of Pomeroy and Dion (1996), a more physically-realistic parameterisation of τ_{pixel} dependent on θ is applied in this study:

$$\tau_{pixel} = \exp(-\kappa_{pixel} \mathrm{PAI}_{pixel} / \sin\theta) \quad (11)$$

where κ_{pixel} and PAI_{pixel} are the same as κ_F and PAI_F but representative across the entire pixel; Thyer et al. (2004) applied this algorithm within the UPC DHSVM application, but defined canopy density through map estimates of F instead of PAI.

The amount of long-wave radiation absorbed at the snow surface (L^*) is:

$$L^* = v_{pixel} L_\downarrow + (1 - v_{pixel})\sigma T_c^4 - \sigma T_s^4 \quad (12)$$

where the first term represents the longwave contribution from the sky and is proportional to the sky-view factor v_{pixel} (i.e., the fraction of the celestial hemisphere visible from the surface; Sicart et al., 2004), the second term is the longwave contribution from the canopy dependent on the Stefan–Boltzman constant σ and canopy temperature T_c assumed equal to T_A, and the last term is the upward longwave flux emitted by the snow surface as a function of temperature, T_s. The canopy and snow emissivity are both assumed equal to unity, which may slightly overestimate the value of the second and third terms, but these errors would offset each other in calculations of L^*.

3. Study area

Baker Creek is located on the Fraser Plateau in central British Columbia (Fig. 1; see online version for colour format), and drains into the Fraser River at Quesnel. The catchment is 1570 km^2 in area with elevations ranging from 480–1530 m, although 80% of this area (1256 km^2) lies between the (hypsometric) H_{90} and H_{10} values of 901 and 1308 m respectively, with a corresponding mean slope angle of 3°. This gentle rolling topography is representative of the wider plateau, with forest cover dominated by lodgepole pine (*Pinus contorta*) located primarily within the Sub Boreal Pine Spruce (SBPS) biogeoclimatic zone, but small areas of white spruce (*Picea glauca*) are also found in relatively wet lowland sites (B.C. Forest Practices Board, 2007). Aerial surveys by the BC Ministry of Forests and Range estimated the fraction of MPB-affected forest across Baker Creek to be less than 2% in 2000 (herein termed 'pre-MPB' conditions), and thereafter rates increased dramatically. Our forest inventories from 2008 did not detect any mature pine-dominated stands with more than half of the trees (weighted by basal area) remaining healthy, and typically only one fifth remained. 34% of the forest has been harvested since the 1960's (B.C. Forest Practices Board, 2007), and logging activity now occurs throughout the catchment. Existing clearcut areas expand by logging around the periphery, and clearcuts or regenerating areas often exceed 100 ha (1 km^2) in size, but none of the previously-anticipated huge clearcuts exceeding 1000 ha in size (B.C. Ministry of Forests, 2004) have occurred to date.

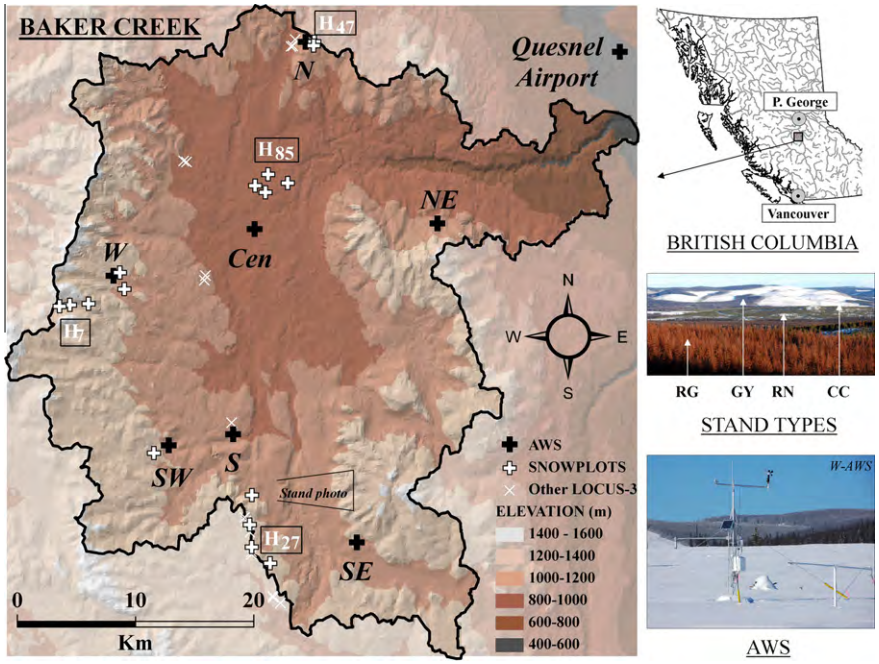

Fig. 1. Location, topography (shown with hillslope illumination effect), representative stand types and AWS in Baker Creek catchment.

The climate of Baker Creek is relatively cool and dry due to its interior location in the shadow of the Coast Mountains. Permanent snowcover usually exists from early November until March at lower elevations, or until April and even May higher up. Daily air temperature and precipitation measurements taken at 915 m inside the catchment between 1975 and 2007 (Environment Canada station 1086550) indicate mean annual precipitation to be 540 mm, 34% of which falls as snow, and monthly average temperatures ranging from −9 °C in January to 14 °C in July. The 45-year period of hydrometric data collected by the Water Survey of Canada at the outlet indicate that the spring freshet typically occurs between mid-April and mid-May each year. Seven of the eight highest annual peak flows all occurred after 1997 (range 70–116 $m^3 s^{-1}$), and numerous anecdotal observations summarised by Summit Environmental Ltd. (2007) suggest that annual spring flooding of the flat catchment interior has occurred since the onset of MPB, imposing major constraints on agricultural (and other) activities such as hay production.

4. Data preparation

In this section, the methods used to obtain the three main spatially-distributed datasets required to run DHSVM, including topography, forest cover and meteorology, are described for Baker Creek. The strategy for measuring Snow Water Equivalent (SWE), used in the subsequent section to calibrate distributed simulations of snow accumulation and to verify distributed simulations of snow melt, is also outlined here.

4.1. DEM

The Baker Creek DEM with 25 m grid spacing was obtained online from the GeoBC website (http://www.geobc.gov.bc.ca, accessed 9th November 2008). Cells were then bi-linearly interpolated to a resolution of 200 m, creating a final input DEM of 39,795 individual pixels on which the model was run.

4.2. Forest cover

The spatial distribution of forest cover across Baker Creek was estimated from 30 m Landsat data, available for 2000 from the Canada Center for Remote Sensing (CCRS, 588 Booth Street, Ottawa, Ontario, Canada, K1A 0Y7), and for 2008 from the USGS Earth Resources Observation and Science (EROS) web portal (http://glovis.usgs.gov/). Land was classified into the seven categories of land use which covered at least 1% of the catchment area in 2008 and for which physical characteristics had either been measured or estimated, as outlined below. The categories include clearcut stands (code CC in Table 2), and four different treed stands including young regenerating pine stands 7.5–15 years old (code RN), juvenile pine stands 16–50 years old (code RG if infested; code RH if healthy), mature pine-dominated stands 51+ years old (code GY if infested and essentially dead; code GN if healthy) or spruce-dominated stands (code SP). Clear structural differences in terms of stand height and stage of beetle kill were present for each age-group, in 2008 (Table 2). For the purposes of this study, any lake or wetland areas were reclassified as clearcut (i.e., bare) areas. The data were interpolated to 200 m resolution using a nearest neighbour approach, and the resulting cell size of 4 hectares is smaller than average stand sizes across the catchment and reduces the proportion of land area classified incorrectly. The final classified land covers are presented in Fig. 2 (see online version for colour format), and all measurement sites in 2007–2009 were checked to ensure correct stand classification within the 2008 dataset.

The values displayed in Table 2, used to parameterise each classified pixel in the model, were obtained as follows. For categories RN, RG and GY, the canopy structural parameters introduced in Section 2, including PAI_{pixel} and v_{pixel}, were both estimated from hemispherical photographs taken every 10 m across a 50 m × 50 m grid using a Nikon Coolpix 4500 camera with FC-E8 fisheye converter, and analysed using the HemiView software (Delta-T Devices, 1999). Parameters H and F were both derived from airborne lidar (light detection and ranging) scanning of numerous 50 m × 50 m plots within Baker as part of a corresponding study,

Table 2
Parameter values applied for each stand type in DHSVM. Height values in brackets represent the field inventory measurements of the dominant overstorey layer but are only shown for comparison purposes. Values for GN are assumed equivalent to values for GY except those in italics, obtained from Spittlehouse (2006).

Group	Parameter	Units	Stand class						Origin of non-GN data
			cc & Bare	RN	RG & RN	GY	SP	*GN*	
Vegetation	Plant Area Index, PAI_{pixel}	m^2/m^2	0.0	0.30	1.34	1.66	2.59	2.40	Measurements (fisheye photos)
	Canopy height, H	m	0.0	$1.5_{(3)}$	$5.7_{(11)}$	$13.1_{(20)}$	$7.8_{(13)}$	13.1	Measurements (LIDAR)
	Fractional Coverage, F	–	0.0	0.12	0.47	0.21	0.56	0.4	Measurements (LIDAR)
	Sky-View Factor, v_{pixel}	–	1.0	0.73	0.26	0.23	0.14	0.18	Measurements (fisheye photos)
Interception	Maximum snow interception capacity, M	m SWE				0.004			Whitaker et al. (2003)
	Minimum melt needed for mass release, D_{min}	m SWE				0.002			Storck (2000)
	Snow mass release/drip ratio, M/D	–				0.4			Storck (2000)
	LAI multiplier for snow	–				0.005			Storck (2000)
Radiation	Pixel shortwave attenuation, κ_{pixel}	–	0.0	0.32	0.4	0.42	0.39	0.42	Field calibrated
	Initial (fresh) snow albedo- α_0	–				0.85			Field calibrated
	Snow Albedo- coefficient A ($T_s < 0$ °C)	–	0.98	0.98	0.95	0.96	0.96	0.96	Field calibrated (assumed values in italics)
	Snow Albedo- coefficient A ($T_s = 0$ °C)	–	0.86	0.86	0.83	0.84	0.84	0.84	Field calibrated (assumed values in italics
	Snow Albedo- coefficient B ($T_s < 0$ °C)	–	0.55	0.55	0.51	0.52	0.52	0.52	Field calibrated (assumed values in italics)
	Snow Albedo- coefficient B ($T_s = 0$ °C)	–	0.43	0.43	0.49	0.45	0.45	0.45	Field calibrated (assumed values in italics)
	Soil albedo					0.10			Whitaker et al. (2003)
	Vegetation albedo	–				0.15			Whitaker et al. (2003)
Aerodynamic	Fractional trunk space height	–				0.5			Whitaker et al. (2003)
	Aerodynamic attenuation coefficient	–				2.0			Whitaker et al. (2003)
	Soil Roughness	m				0.01			Whitaker et al. (2003)
	Snow Roughness	m				0.004			Spittlehouse and Winkler (2002)
Other	Snow Water Holding Capacity	%				1.0			Spittlehouse and Winkler (2002)
	Maximum Snow Surface layer depth	m SWE				0.125			University of Washington (2006)
	Maximum air temperature for snow	°C				3.3			US Army Corps of Engineers (1956)
	Minimum air temperature for rain	°C				−1.1			US Army Corps of Engineers (1956)

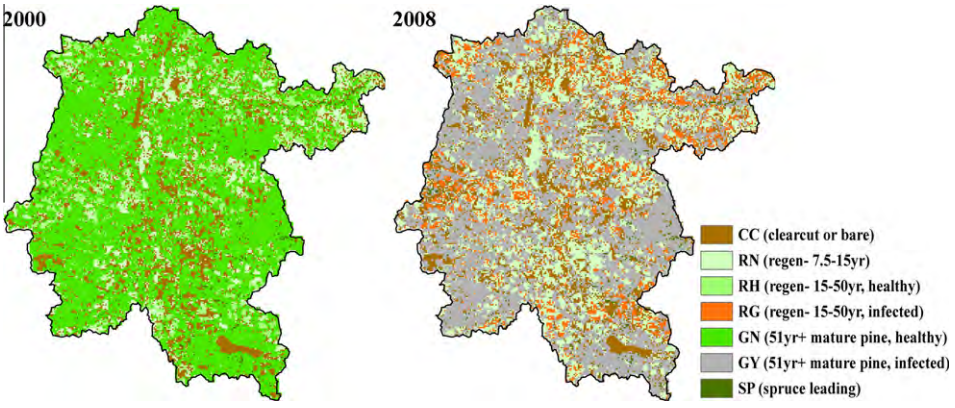

Fig. 2. Classified land cover for Baker Creek SWE simulations in 2000 (pre-MPB) and 2008.

with tree core measurements used to assign each analysed lidar plot within an age category for this study. Resulting values of both H and F (Table 2) are lower than would be obtained from standard field measurements of the top canopy layer alone, and are more representative of a single canopy layer. Values for the two parameters I_e and κ_{pixel} are described in the model calibration section, and remaining parameter values required by the model were derived from other forest studies and held constant between the land categories (Table 2).

In the 2000 land cover, all classified pixels with pine stands 16–50 and 51+ years old in the 2000 dataset were assumed healthy based on extensive anecdotal observations, and were therefore classified as RH and GN stands respectively. No healthy stands were present in 2008, however, to measure and parameterise these within the model. Structural values for GN stands were estimated, therefore, by using PAI_{pixel}, v_{pixel}, and F values measured in other healthy mature stands prior to MPB (Spittlehouse, 2006), and H was not assumed to change due to MPB. The structural values for RH were assumed equal to the attacked values for RG given that these stands were only in the initial stages of defoliation.

4.3. Meteorology

A network of seven Automatic Weather Stations (AWS) has been operating in Baker Creek since June 2007, each one located in a recent clearcut, on relatively flat ground of up to 4° slope,

and are named according to their relative geographic position within the catchment (Fig. 1). Additional data measured by Environment Canada at Quesnel Airport (station 1096625; elevation 545 m a.s.l.) are also used and improve the representation of weather data particularly across the lower, northeast corner of the catchment extending towards the outlet in Quesnel. The elevations covered by all 8 AWS range from 545 m to 1206 m a.s.l., which covers the 70% of basin area lying above the outlet (H_{98}–H_{28}).

The meteorological variables required by DHSVM were measured at the Baker AWS using the following sensors: Vaisala HMP45C (T_A and RH), RM Young 5103 (U), Kipp and Zonen CMP3 ($K_\downarrow$) and CGR3 ($L_\downarrow$), Texas Instruments TE525 M (P in summer) and Campbell Scientific SR50/a (P in winter). T_A, RH, $K_\downarrow$ and U were measured on an hourly basis at each AWS, at heights of 2 m except for U at 4 m and these data were reduced by extrapolation down to 2 m using the standard logarithmic wind-speed equation in neutral stability and an assumed snow surface roughness of 0.004 m after Thyer et al., 2004. $L_\downarrow$ was measured throughout the simulation period at W-AWS (1206 m), and at Cen-AWS (903 m) during April and May 2009; the resulting 48-day period of simultaneous data was then used to determine the linear relationship $L_{\downarrow \text{Cen-AWS}} = 1.030\ L_{\downarrow \text{W-AWS}}$ ($R^2 = 0.85$), which represents an increase of 0.99% in measured $L_{\downarrow \text{W-AWS}}$ for every 100 m decrease in elevation and is the function used to obtain $L_\downarrow$ for all other AWS. For precipitation input at each AWS, snowfall (water equivalent) was estimated from minimum increases to hourly snow depth measurements using a method described in the calibration section, and any rain was measured using a tipping bucket rain gauge, although rainfall events were uncommon during the study period. SWE was also periodically measured next to each AWS using a standard Federal snow tube with diameter of 4.13 cm. At Quesnel Airport, T_A, RH, U and P (all seasons) were measured directly, $L_\downarrow$ was estimated from $L_{\downarrow \text{W-AWS}}$ corrected for elevation, and $K_\downarrow$ was taken from the nearest Baker AWS (NE) without modification. Like $L_\downarrow$, T_A and P were made to vary with elevation using a lapse rate that was calibrated monthly (but not spatially) using average AWS measurements (Table 3), whereas RH, U and $K_\downarrow$, do not necessarily vary with elevation and were interpolated using the inverse distance scheme described by Wigmosta et al. (2002).

Table 3
Calibrated lapse rate values of T_A, P, and *SF-Threshold* and I_e applied within the model, along with mean values of $SWE_{T/CC}$ used in the calculations of I_e. The GN $SWE_{T/CC}$ value of 0.75 was taken from Spittlehouse (2006).

Parameter	2008		2009	
Meteorology lapse rates	T_A (°C/km)	P (m.w.e./km)	T_A (°C/km)	P (m.w.e./km)
November	−3.8	0.7	−3.7	4.2
December	−0.7	0.3	−1.4	−1.2
January	0.8	1.8	2.0	0.2
February	2.7	0.2	0.9	−0.7
March	−3.8	0.7	−3.9	1.0
April	−5.8	10.0	−4.6	−0.3
May	−5.5	−0.1	−5.5	1.4
SF-Threshold (mm depth)				
Cen-AWS	4.25		6.00	
W-Cen	5.75		3.75	
SW-AWS	3.75		9.25	
S-AWS	2.25		6.50	
SE-AWS	3.50		2.25	
NE-AWS	3.50		7.00	
N-AWS	8.25		3.50	
Interception	$SWE_{T/CC}$	I_e	$SWE_{T/CC}$	I_e
RN	1.06	0.07	1.06	0.05
RG	0.94	**0.11**	0.92	0.22
GY	0.84	0.20	0.98	0.16
SP	0.87	0.10	0.87	0.15
GN	0.75	0.25	0.75	0.32

4.4. SWE

A spatial network of snow survey plots was formed to monitor SWE variability across Baker in both winters, with the data used not only to calibrate model snow accumulation differences (using a method outlined in the subsequent section), but also to verify simulated melt rates. The network incorporated only forest cover and elevation effects on SWE variability; slope and aspect effects were minimised by locating all plots on relatively flat ground of up to 6° slope (the catchment average is 3°). Forest cover was segregated into the four predominant stand classes covering the MPB landscape (CC, RN, RG and GY; Fig. 1), and elevation was divided into four bands, with plot clusters located at mean values of 920 m (H_{85}), 1110 m (H_{47}), 1215 m (H_{27}) and 1325 m (H_7), situated in the catchment interior and towards the northern, southern and western catchment boundaries respectively (Fig. 1). Plots within each cluster did not exceed a maximum difference of 30 m elevation or 5 km distance in order to minimise the potential snowpack variability from different meteorological forcing. A suitable RN plot could not be found at the H_{47} and H_7 levels, or a GY plot at the H_{47} level, leading to a final stratified landscape design including 13 plots. A further five plots were setup to supplement this design; two additional clearcut plots in 2009 used to test replication of the H_{85} and H_{27} clearcuts located 4 and 6 km away respectively, and an additional cluster adjacent to W-AWS used specifically for detailed energy balance studies (sites EB-RG and EB-GY). Table 4 summarises the stand characteristics for all 18 plots, and the mean of individual plot values of PAI_{pixel}, v_{pixel} and H form the class-mean average values applied within the model (Table 2).

Each plot was 50 m × 50 m (0.25 ha) in size, consisting of 36 stake locations spaced 10 m apart. Snow depth measurements at each stake were multiplied by the mean snow density value averaged from five snowtube measurements obtained at each corner and in the center, to generate 36 SWE values per plot from which the mean was calculated. Variogram analysis of 1 m spaced depth measurements as part of a pilot study in 2007 indicated that a 10 m sampling resolution was sufficient to avoid underestimating plot snow depth variance due to spatial autocorrelation, for all stand types. An entire catchment snow survey of 13 plots (15 in 2009 with two replicates) took between 1.5 and 2.5 days to complete, using two independent teams of two people in 2008 and one team of two people in 2009, and no known snowfall or strong ablation events were thought to occur within the space of the accumulation-period surveys. During melt, only one landscape survey was possible in 2009, and this shortfall was addressed by placing a battery-powered LOCUS-3 prototype ultrasonic range sensor in each of the H_{85} and H_7 study sites for automated snow depth measurements through the 2009 melt period. Testing of the LOCUS-3 snow depth data against the Baker AWS data in 2009 indicated a high degree of measurement accuracy. Plot SWE values were estimated from the LOCUS-3 data by extrapolating the point snow depths across the plot using the method outlined by Neumann et al. (2006), and these data were multiplied by the interpolated plot-average snow density values (maximum limit 400 kg m^{-3}) derived from the peak and melt surveys. The resulting SWE values were averaged daily for comparison against model simulation data.

4.5. Other distributed data

The ability of DHSVM to simulate spatial snowpack dynamics across Baker can be verified against patterns of snow-covered area (SCA) measured by the Moderate Resolution Imaging Spectroradiometer (MODIS), available from the National Snow and Ice Data

Table 4
Individual plot characteristics used for snow and canopy measurements. Values are in plain text for clearcut (CC) stands, in italics for regenerating (RN) stands, underlined for attacked regenerating stands (RG) and in bold for dead mature ('grey') stands.

Stand		Topography			Forest cover								
ID	Class	Elevation	Slope	Aspect	PAI_{pixel}		v_{pixel}		Stems	Basal area	Height	Pine	MPB
		m.a.s.l.	0		Mean	C.V.	Mean	C.V.	N/ha	m/ha	m	%	%
H_{85}-CC	CC	921	<2		(0)	–	(1)	–					
H_{85}-RN	*RN*	*924*	<2	–	*0.07*	*0.21*	*0.91*	*0.02*	*1750*	*2*	*1.2*	*100*	*0*
H_{85}-RG	RG	924	<2	–	1.10	0.17	0.31	0.16	2000	15	10.6	93	23
H_{85}-GY	**GY**	**927**	**<2**		**1.17**	**0.13**	**0.30**	**0.12**	**1375**	**32**	**19.4**	**96**	**99**
H_{47}-CC	CC	1106	2.5	SE	–	–	–	–	–	–	–	–	–
H47-RG	RG	1109	5	NE	1.33	0.10	0.26	0.09	2850	32	13.1	77	86
H_{27}-CC	CC	1221	<2	–	–	–	–	–	–	–	–	–	–
H_{27}-RN	*RN*	*1234*	*<2*	–	*0.53*	*0.65*	*0.55*	*0.30*	*2867*	*3*	*2.5*	*100*	*2*
H_{27}-RG	RG	1203	<2	–	1.41	0.09	0.24	0.07	1075	18	11.9	97	97
H_{27}-GY	**GY**	**1217**	**<2**	**–**	**1.78**	**0.16**	**0.21**	**0.16**	**1800**	**55**	**21.5**	**76**	**100**
H_7-CC	CC	1315	3.5	SSE	–	–	–	–	–	–	–	–	–
H_7-RG	RG	1339	<2	_	1.28	0.17	0.28	0.18	2275	16	8.5	88	15
H_7-GY	**GY**	**1323**	**4**	**SSE**	**1.87**	**0.09**	**0.19**	**0.10**	**1950**	**54**	**19.1**	**69**	**97**
H_{85}-CC-REP	CC	903	<2	–	–	–	–	–	–	–	–	–	–
H_{27}-CC-REP	CC	1244	<2	–	–	–	–	–	–	–	–	–	–
EB-CC	CC	1206	4	S	–	–	–	–	–	–	–	–	–
EB-RG	RG	1201	4	sw	1.59	0.12	0.21	0.16	1700	18	9.8	98	83
EB-GY	**GY**	**1166**	**<2**	**–**	**1.82**	**0.14**	**0.20**	**0.14**	**2033**	**48**	**19.3**	**89**	**95**
SP1	SP	*1013*	<2	–	*2.59*	*0.19*	*0.14*	*0.25*	*6700*	*46*	*13.0*	*28*	*59*

Center web interface (Hall et al., 2000; http://nsidc.org/data/snowi/). In other studies, over 90% of snow-covered pixels were correctly classified in forest areas when snow depths exceeded 1 cm (Ault et al., 2006; Hall and Riggs, 2007), although the 500 m pixel resolution does not permit the model accuracy to be determined in this study for individual 200 m pixels. Instead, the regional distributions of simulated SCA can be validated using this data. Three days with minimal cloud cover were selected for model comparison during melt, including 22-April and 6-May in 2008, and 28-April in 2009, and these dates correspond within ±2 days of the snow surveys (or automated measurements) which also provide ground-based data on snowcover status.

The soil distribution, road and stream networks also required to run DHSVM do not form an integral part of this particular study and are not discussed further, but soil surface albedo and roughness values were required to complete energy-balance calculations, and these were assumed constant across the catchment (0.1 and 0.01 m, respectively) after Whitaker et al., 2003. Previous soil surveys suggest only limited spatial variability of soil properties across the catchment (Lord and Mackintosh, 1982).

5. Model calibration

This section outlines the individual methods used to calibrate model calculations of snow accumulation in clearcuts and treed stands, and the subcanopy radiative fluxes, with which to improve the accuracy of simulated spatial and temporal SWE distributions across the catchment.

5.1. Clearcut snow accumulation

Time-series of winter precipitation amounts for input into DHSVM were estimated from the measured increases in snowdepth made by the SR50/a sensor at each Baker AWS; a method common to studies without direct precipitation measurements (e.g., Thyer et al., 2004; Jost et al., 2009). The uncertainties in fresh snowfall depths due to effects on sensor performance such as snowfall intensity, crystal structure and strong winds (Brazenec, 2005) were reduced by firstly compensating the distance readings for air temperature, then removing large individual spikes within the data, then smoothing the data using a 3-h moving average, and finally introducing a minimum snowfall depth threshold ('*SF-Threshold*') above which snowfall was assumed to occur. The resulting snowfall depths were multiplied by an assumed density of 100 kg m^{-3} for fresh snowfall, to estimate snowfall water equivalent (winter precipitation) amounts. Values of *SF-Threshold* were then adjusted within model runs until the simulated SWE at each of the seven AWS pixel locations was within ±5% of the corresponding SWE measurements obtained at or just prior to the maximum snowpack, and Fig. 3 shows the resulting time-series of precipitation and SWE at W- and Cen-AWS in both years. Final calibrated values of the *SF-Threshold* depth are shown for individual AWS in Table 3.

5.2. Snow albedo

Thyer et al. (2004) first introduced distinct *A* and *B* coefficient values into Eq. (8) to simulate different albedo decay rates in open and treed pixels at Upper Penticton Creek. In the current study, pyranometer measurements of snow albedo were available to calibrate specific decay curves for a representative RG and GY stand, and two CC stands, but not RN stands and the mean CC function was applied at RN stands in the model simulations. Time series of snow albedo in 2009 were calculated from the ratio of reflected to incident solar energy fluxes summed each day, and filtering out unrealistic values of $\alpha_s > 0.95$ (CC) and $\alpha_s > 0.9$ (RG and GY) most likely due to fresh snowfall lying on top of the upward-looking pyranometers. To correct the data for the presence of trunks, all remaining values for RG and GY stands were then increased by small values of 0.024 and 0.023 respectively, calculated from trunk positioning in downward fisheye images taken towards the end of melt, the cosine response of the pyranometers, and realistic estimates of snow and trunk albedo. Finally, individual decay curves measured at each plot between snowfalls were organised into melting and non-melting phases, with final optimised curves representing those which minimised the overall Root Mean Squared Error (RMSE) of individual curves; coefficient values are shown in Table 2, with clearcut values taken as the average from the two clearcuts. The measurements and resulting decay curves indicate that during freezing conditions, almost no albedo decay occurred in the clearcuts, similar to measurements above continuous snow in the Canadian Prairies (Pomeroy et al., 1998), and albedo decay

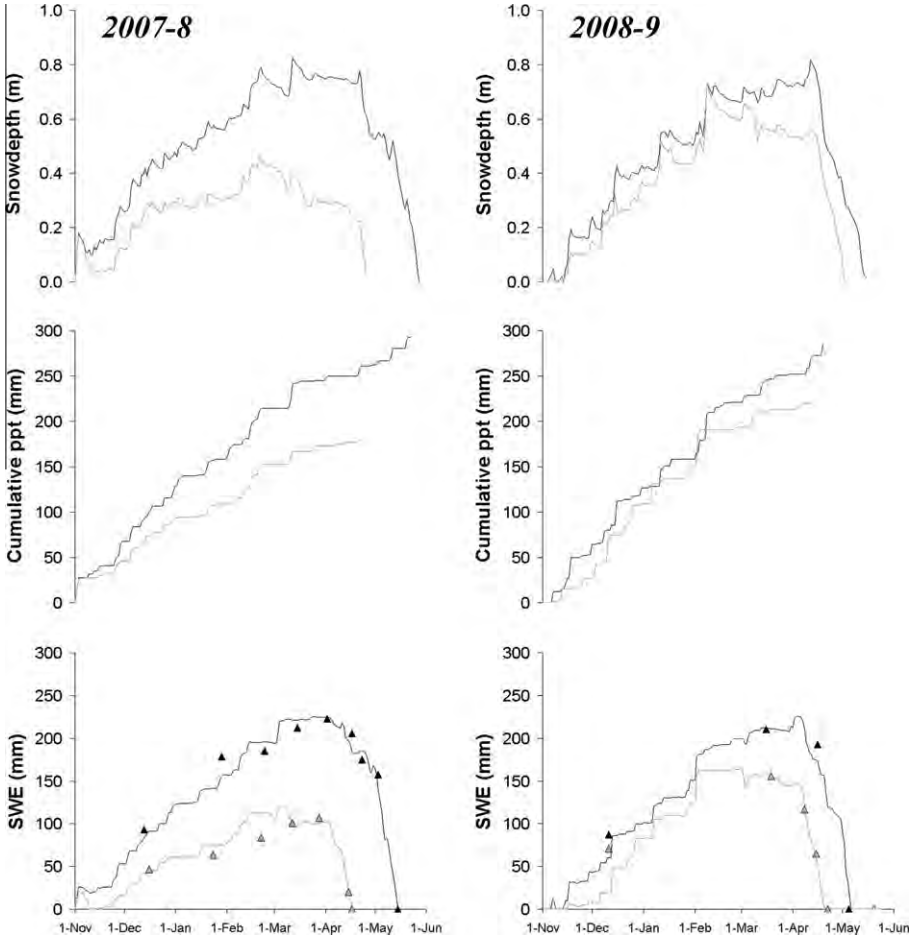

Fig. 3. Time series of measured snowdepths (top), estimated cumulative precipitation (middle), and measured and model simulated SWE (bottom), for W-AWS (1206 m a.s.l.; black) and Cen-AWS (903 m a.s.l.; grey).

was also slowest in the clearcuts during melt. The decay rate was fastest in the RG stand, where more litter was typically present under the radiometers due to the recent stage of MPB attack. Unpublished data of surface litter fractions in this plot, determined from spatial photo analyses, indicates that the maximum recorded litter fractions reached ~0.4 during melt when successive litter layers became exposed.

5.3. Subcanopy irradiative fluxes

Subcanopy solar irradiance is simulated in this study by Eq. (11), using known values of θ, class-specific PAI_{pixel} values (Table 2), and extinction coefficient κ_{pixel} values optimised for each stand class using the following method. Firstly, the most representative plot for each stand class was identified (i.e., of closest PAI_{pixel} value to the class mean in Table 2), for which mean half-hourly values of τ_{pixel} were estimated using Hemiview software analysis of the 36 individual fisheye photos. These τ_{pixel} data and known values of θ were then applied within Eq. (11) rearranged to solve for κ_{pixel},

$$\kappa_{pixel} = \sin\theta \log \tau_{pixel}/PAI_{pixel} \quad (13)$$

Calculated κ_{pixel} values between the hours of 09:00–15:00 (when solar irradiance was highest) were then averaged for each month during the snow-covered season of November through May, and Table 5 summarises the variability in calculated κ_{pixel} and τ_{pixel} values, between stand types but also temporally by including the seasonal average values and individual values for April (assumed to be the most important month for subcanopy melting). The results indicate that for either time period, τ_{pixel} decreased from the RN stand, to the RG and GY stands, although calculated κ_{pixel} values were similar (0.31–0.33 for season-long values), a feature identified in other stand comparisons (e.g., Sicart et al., 2004). κ_{pixel} and τ_{pixel} values were both higher in April than averaged across the snow-covered season, which indicates the dependence of shortwave transmission on solar and canopy geometry.

Table 5
Plot mean values of PAI and τ used within Eq. (13) to calibrate values of κ across the winter and for April. Standard deviation values shown in italics.

Class (plot used)	PAI_{pixel}	τ_{pixel}		κ_{pixel}	
		November–May	April	November–May	April
RN ($H_{1220\text{-}RN}$)	0.53	0.60	0.76	0.31	0.32
	0.34	*0.15*	*0.05*	*0.03*	*0.07*
RG ($H_{1220\text{-}RG}$)	1.41	0.30	0.40	0.31	0.40
	0.13	*0.09*	*0.05*	*0.10*	*0.05*
GY ($H_{1220\text{-}GY}$)	1.78	0.20	0.30	0.33	0.42
	0.29	*0.09*	*0.05*	*0.09*	*0.03*

A comparison of τ values measured and simulated at individual points in the EB-RG and EB-GY stands where pyranometers were located enable the accuracy of optimised κ_{pixel} values in Table 5 to be assessed for independent locations. Measured τ values were calculated as the ratio of subcanopy to adjacent clearcut (W-AWS) values, whereas simulated τ values using Eq. (11) apply the various

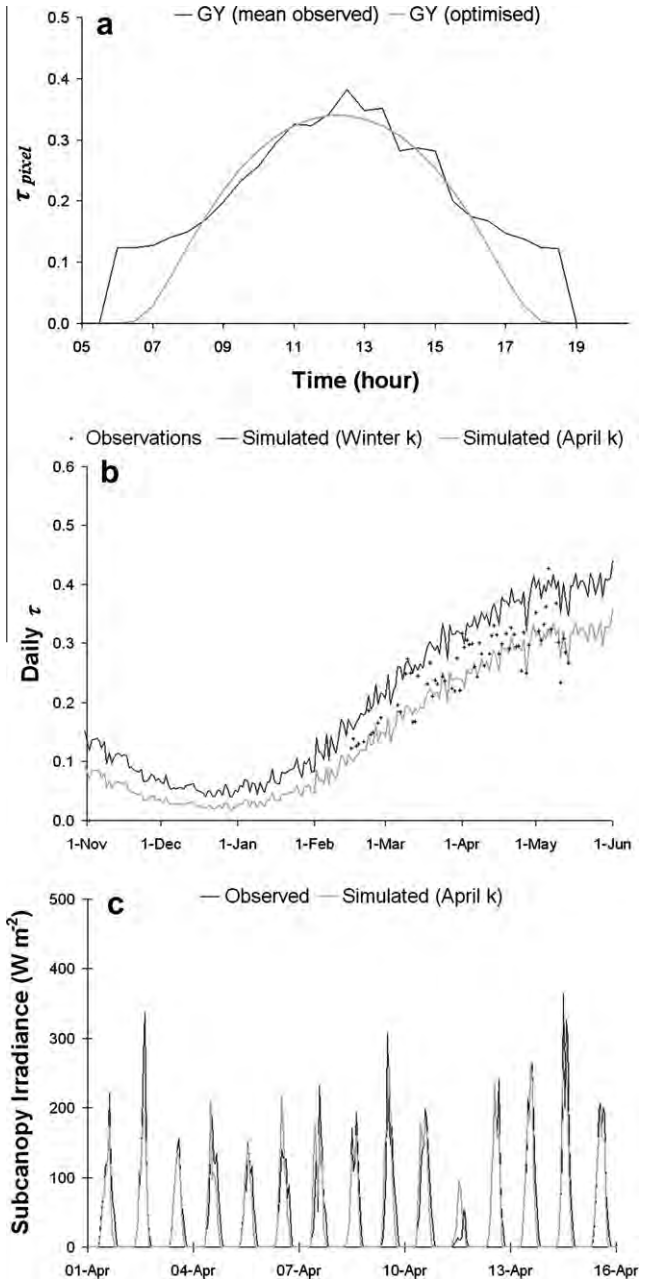

Fig. 4. (a) Hourly values of τ_{pixel} averaged from fisheye measurements across a GY-stand in April, and the τ_{pixel} scheme optimised from Eq. (11) and applied within the model. (b) Comparison of simulated subcanopy solar irradiance against pyranometer measurements from EB-GY (Fig. 3), averaged daily across the 2008 snow season and (c) for an hourly subset in April 2008.

κ_{pixel} values in Table 5 together with the PAI values specific to each pyranometer location (1.71 at EB-GY, 1.42 at EB-RG). Results are displayed in Fig. 4 for site EB-GY, and indicate that simulated daily τ values reproduce the seasonal increase of τ measured reliably from February onwards, but applying the κ_{pixel} value optimised for April yields lower error (RMSE = 0.05τ) than the seasonal value which generally overestimates τ (RMSE = 0.08τ). The reverse would likely be true prior to February when θ was low, although errors in modelled solar transmission during mid-winter using the April κ_{pixel} value would be limited by the low solar fluxes present during this period.

For model simplicity, a single κ_{pixel} is sought for each class, and the April-optimised values from Table 5 are those chosen for application within DHSVM. Using these values, hourly τ simulations during the first half of April 2008 (Fig. 4) are in general agreement with measured values (RMSE = 39 W m^{-2}), although some daily peaks are intermittently missed as would be expected when a κ_{pixel} value optimised spatially at the plot scale and temporally at the month scale is applied within hourly simulations at a single point within the stand. Additional small sources of common model error such as the absence of multiple scattering are described more fully by Nijssen and Lettenmaier (1999). The corresponding seasonal and hourly τ RMSE errors at EB-RG were 0.10 τ and 45 W m^{-2} respectively.

Longwave subcanopy irradiance $L_{\downarrow}$ is simulated as the sum of sky and canopy longwave contributions (first and second terms of Eq. (12)), and pyrgeometers located next to the pyranometers outlined above between mid-March and mid-May 2008 enable the model accuracy to be assessed. Measured values of T_A (assumed equal to T_C) and sky-view factor were applied in Eq. (12) to simulate $L_{\downarrow}$ at each pyrgeometer location. Hourly estimated values were in close agreement with measurements, with RMSE errors of 7.5 W m^{-2} (RG) and 6.0 W m^{-2} (GY) that are similar to those obtained in healthy pine canopies using the same method (Pomeroy et al., 2009). Measured daily sums of $L_{\downarrow}$ were higher by 1–38% in the subcanopy locations relative to the clearcut, and increased under clear-sky conditions as would be expected due to the larger difference in canopy and sky emissivities during these periods (e.g., Sicart et al., 2004).

5.4. Subcanopy snow accumulation

Subcanopy snow accumulation was calibrated by simply fine-tuning the values of I_e in the canopy snow model (Eq. (1)) until simulated ratios of treed stand to clearcut SWE (herein defined $SWE_{T/CC}$) for each class and winter season matched the average of corresponding measurements obtained in the peak-SWE snow surveys, shown in Fig. 5. This method therefore integrates the fine scale changes in I_e that occur spatially within an individual class between stands of different density, and temporally between snowfall events of varying size (e.g., Hedstrom and Pomeroy, 1998).

Final values of I_e applied within DHSVM appear in Table 3, and the corresponding $SWE_{T/CC}$ measurements indicate that young regenerating (RN) stands accumulated slightly more SWE than clearcuts in both winter periods ($SWE_{T/CC}$ = 1.05), whereas attacked stands (RG) accumulated 6% and 8% less in 2008 and 2009 respectively. SWE in dead mature (GY) stands exhibited wider annual variability, with near-equal amounts in 2009 ($SWE_{T/CC}$ = 0.98) but less in 2008 ($SWE_{T/CC}$ = 0.84). For reference, the measurement of $SWE_{T/CC}$ = 0.75 by Spittlehouse (2006) was used to simulate peak SWE in the healthy mature (GN) stands as part of the pre-MPB (2000) land cover.

The RG and GY ratios are generally slightly higher than the average values calculated by Winkler and Boon (2009) using all MPB studies from the Interior Plateau ($RG_{10–40\ year}$ = 0.84 and $GY_{40+\ year}$ = 0.875), but the range of individual values varied considerably more (e.g., between 0.42 and 1.28 for $GY_{40+\ year}$ stands; Winkler and Boon, 2009). Only two of the stand comparisons in Fig. 5 were statistically significant at the p = 0.05 level, as indicated by no overlapping of the median values within the interquartile ranges (see Boon, 2007), including the CC and GY stands at 1330 m a.s.l., and RN with CC and GY stands at 1220 m a.s.l., both occurring in 2008. This lack of stand variability would be less likely to occur in much lower snow years when variations in snow accumulation are enhanced (e.g., Boon, 2007); peak SWE values measured at nearby Nazko Station 1C08 were near-normal in 2008 and 30% higher than normal in 2009 (B.C. Ministry of Environment, 2009).

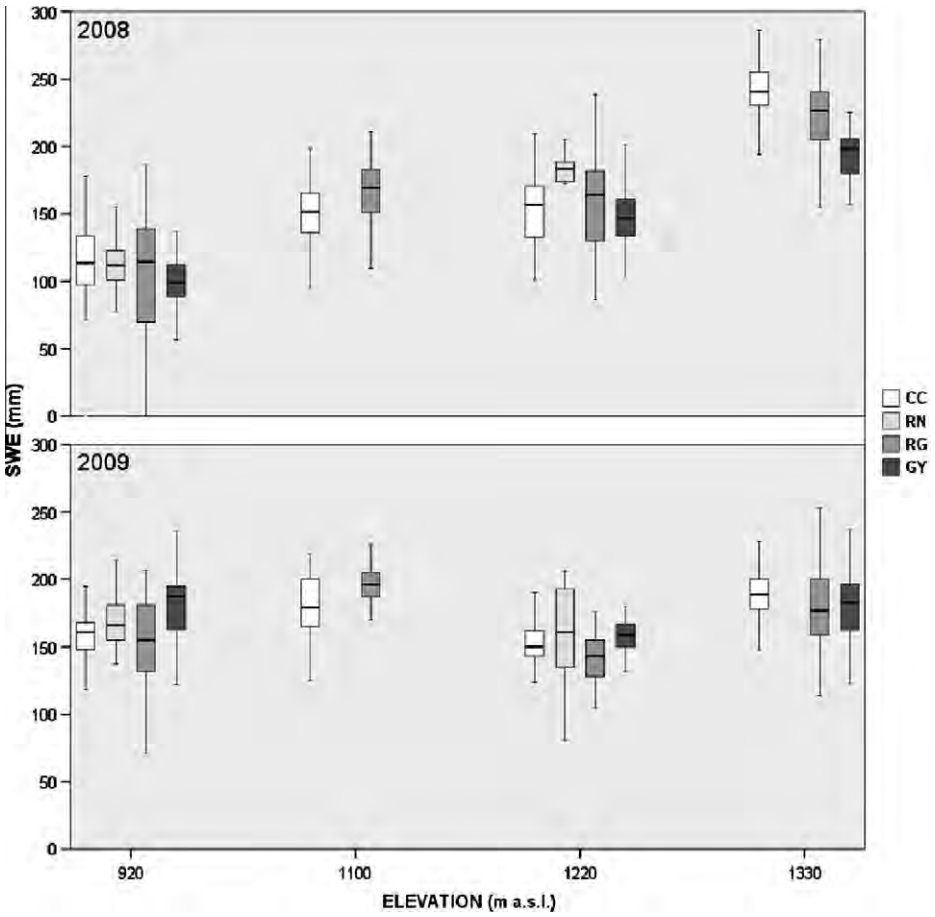

Fig. 5. Peak SWE characteristics measured on 27–28 March 2008 and 18–19 March 2009, arranged in clusters of elevation. The whiskers, box length and central line represent the 10th/90th percentile, 25th/75th percentiles and plot median, respectively.

6. Results and discussion

This section is arranged into three main parts, and evaluates: (i) the model accuracy in simulating pixel (stand level) SWE where grid-based measurements or automated estimates of SWE data were collected, (ii) the accuracy of simulated catchment melting patterns against ground-based or satellite snowcover data, and (iii) a comparison of SWE variability between the pre- and current-MPB landscapes under identical meteorological conditions.

6.1. Stand-level simulations

6.1.1. Clearcuts

The accurate performance of DHSVM SWE simulations at the weather station pixels is indicated in Fig. 3 for W- and Cen-AWS in both years, and this was the case for other AWS locations, with pixels becoming snow-free within two days of the measured SR50 snowdepth data reaching zero, although better performance would be expected due to the direct proximity of forcing weather data and use of calibrated peak SWE and albedo values.

Away from the AWS, model SWE simulations at the H_{85} and H_7 pixels test the model's ability to interpolate the meteorological data over large horizontal and vertical distances, particularly at the H_7 stands which represent a mean vertical increase of 130 m above W-AWS, the nearest weather station located at 1206 m a.s.l. A comparison of model and LOCUS-3 derived SWE measurements is shown in Fig. 6 for the 2009 melt period (see online version for colour format); these results suggest that for stand H_{85}-CC the measured peak SWE on 4-April (167 mm) and ablation rate (9.8 mm d^{-1}) were both underestimated by 20% in the model, leading to close agreement within the dates of snow disappearance (20-April simulated, 21-April measured). Seven and 8% of the simulated snowfall amounts at H_{85}-CC were lost to sublimation in 2008 and 2009 respectively, similar to corresponding values obtained in other open areas with comparable climate regimes (e.g., Suzuki et al., 2006), and percentages were typically 1–2% higher across the upper elevations (e.g. at H_7-CC) where wind speeds were enhanced.

At H_7-CC, the measured peak SWE amount (231 mm on 6-April) and ablation rate (6.3 mm d^{-1}) were both simulated within 3% by the model leading to a common snow-free date of May 10; however, available grid measurements indicate that model clearcut performance in 2008 was worst at H_7-CC, with measured peak SWE of 245 mm on 28-March accurately simulated within 4%. Simulated melting was too slow and the final grid measurement taken on 5-May (165 mm) was overestimated by 59 mm. This could be due to strong non-linearity within the lapse rates of temperature or precipitation for this particular time period or part of the catchment, which was not represented well by using monthly, spatially-invariant lapse rates within the model. Testing and application of a physically-based weather distribution model such as MicroMet (Liston and Elder, 2006) as a sub-component of DHSVM may yield more accurate distributed input data in future studies.

Another potential source of model error, and reason for the increased stand homogeneity within peak SWE relative to traditional forested catchments with healthy canopies and smaller clearcuts

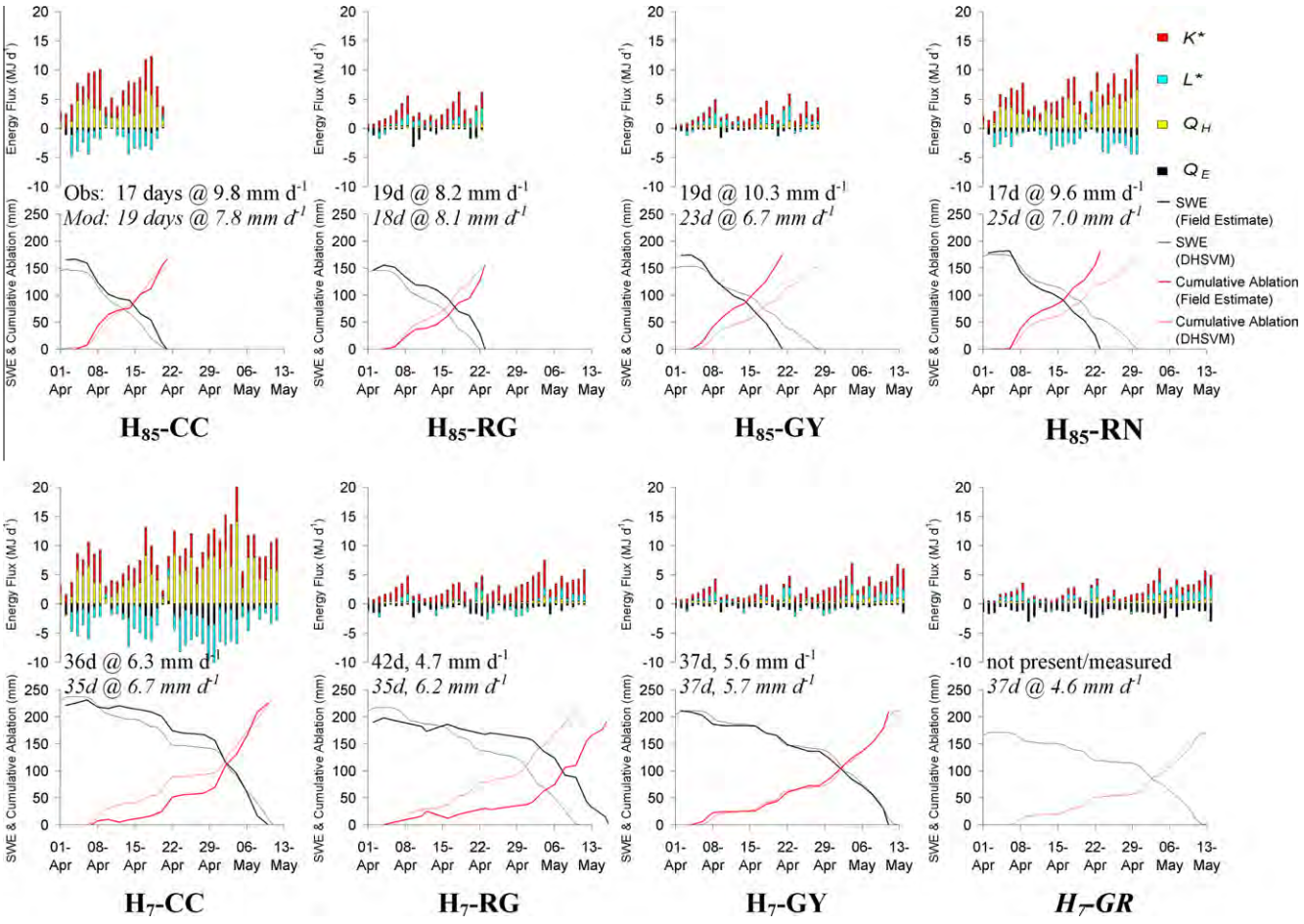

Fig. 6. Top section: simulated energy fluxes in MJ d^{-1} at each H_{85} and H_7 study site in 2009, with corresponding graphs of field estimated (measured) and modelled SWE and cumulative ablation rates in 2009. Stated values represent observed and modelled ablation period lengths and mean daily rates on the upper (bottom) lines.

(e.g., Boon, 2007), is blowing snow transport. Blowing snow transport rates vary with wind speed, air temperature, and snow age over short timescales, and can potentially remove the majority of snowfall from exposed snowcovers in prairie and tundra landscapes (e.g., Pomeroy and Li, 2000; Tabler 1973). Blowing snow processes are not expected in traditional forest environments, however, and therefore are not simulated within forest hydrological models such as DHSVM. No direct measurements of blowing snow transport (e.g., using particle detectors; Jackon and Prowse, 2009) occurred as part of this study, but analysis of the AWS SR50 snowdepth data initially suggests that blowing snow transport may occur for certain combinations of meteorological events, in these larger clearcuts representative of the catchment. In particular, one event occurred on 12-December 2007 when almost all of the 15 cm of fresh snowfall (recorded at Cen-AWS, but similar to other locations) on this date was removed within the subsequent period of several hours when mean and maximum wind speeds consistently exceeded 5 and 10 m s^{-1} respectively. Three other distinct snowfalls occurred during the mid-winter period (when snowmelt was not possible), but winds were light for several days after each event, and subsequent reductions within measured snow depths were most likely due to the snow compaction that occurs from snow metamorphosis and overburden processes (e.g., Anderson, 1976). More targeted measurements are clearly required to verify the presence and effect on seasonal snowpack amounts of blowing snow processes within this environment, with which to parameterise within existing models such as DHSVM or not.

6.1.2. Treed stands

SWE was simulated with varying accuracy among the five sub-canopy stands with continuous SWE data in 2009 (Fig. 6). At H_7-GY, measured peak SWE (211 mm on 2-April), ablation rate (5.4 mm d^{-1}) and meltout date (11-May) were all accurately simulated by the model, but both snow accumulation and ablation were considerably underestimated at H_{85}-GY (by 13 and 38% respectively), with a meltout date that occurred 6 days earlier than in the model. A likely reason for this less impressive model performance here was the application of the mean GY canopy parameter set (Table 2) to this particular stand, which overestimated the actual PAI_{pixel} by 0.49, and v_{pixel} by 0.07 according to fisheye photo analaysis (Table 4). Corresponding values at H_7-GY were much closer to the mean values, with PAI and v_{pixel} under- and overestimated by 0.21 and 0.04 respectively.

The use of spatially invariant, calibrated mean canopy parameter values will inevitably lead to both under- and overestimation of snow accumulation and ablation rates for different treed pixels, and associated research at Baker Creek relating ground data with various remotely-sensed MPB data (including Lidar, Landsat, and AVHRR) will help to spatially distribute and refine the forest cover parameter set for future modelling attempts. A canopy density that was overestimated within the current land cover dataset, like at H_{85}-GY, would account for the overestimated snow interception (measured SWE values were marginally higher than in the clearcut, H_{85}-CC), and ablation rates that were simulated too slow due to an underestimation of the snow albedo decay rate, solar radiation transmission and canopy wind speeds hence turbulent transfer.

The increased canopy longwave emissions due to warming of tree boles above air temperature, outlined by Pomeroy et al. (2009), is not incorporated within the DHSVM model algorithms, but this process would be more likely to occur for lower density stands such as H_{85}-GY, and potentially lead to further model underestimation of the melt rate.

At remaining sites, snow accumulation was correctly simulated as being fractionally higher in the young regenerating plot H_{85}-RN than in the clearcut (H_{85}-CC), although modelled ablation occurred too slowly leading to a snow-free date 6 days later than was observed. Similar to H_{85}-GY, the canopy density was also overestimated here, but the application of a clearcut-calibrated albedo decay curve would additionally underestimate absorbed shortwave radiation due to the limited amounts of snow surface shading, litter and buried vegetation that occur in RN type stands. Conversely, meltout of the snowpack occurred 7 days too early at the high attacked stand (H_7-RG), with canopy density values similar to the stand averages (e.g., $PAI_{pixel} \sim 1.3$), but this stand was only recently infested by MPB leading to lower litter concentrations than were present at site EB-RG from where the calibrated RG decay curve was obtained. In the hypothetical H_7-GN (healthy mature) stand classified as part of the 2000 land cover, the simulated peak SWE of 171 mm occurring on 4-April was 40 and 60 mm less (19% and 26%) than the corresponding measurements from H_7-GY and H_7-CC respectively, and mean daily ablation of 4.6 mm d^{-1} was lower by 0.9 and 1.9 mm d^{-1}, or 17% and 30%. These differences in simulated accumulation and ablation led all three sites to become snow free over the three day period between 10-May (CC) and 12-May (GN). In terms of modelled sublimation, canopy snow sublimation removed 2% of snowfall amounts at GN stands and 1% at GY stands where only limited interception occurred, whereas for both stands a further 4–5% of snowfall amounts (depending on the winter) were sublimated from the subcanopy snowcover.

6.1.3. Energy balances

Fig. 6 also displays the daily sums of energy-balance components simulated at each H_{85} and H_7 site during the main ablation period of 2009. These values represent the fluxes simulated by applying the class mean canopy values, and not the actual canopy values at these locations, but the difference in these values was especially small for each H_7 site. In terms of the relative flux contribution to melt energy (Q_M) during the period in which snow cover remained at all sites (determined to be 4–19 April at H_{85}, and 4-April to 9-May at H_7), the results indicate that K^* was inversely related to class PAI, and L^* increased with PAI changing from negative values in the CC and RN stands, to positive in the RG, GY and GN stands. The contribution of net radiation to Q_M was 42% at H_{85}-CC, 43% at H_{85}-RN, and only 12% at H_7-CC, but ranged between 78% and 118% in the RG, GY and GN stands that indicates the dominance of net radiation as the main source of melt energy in these stands. The contribution of sensible heat flux (Q_H) was larger than net radiation (but not K^*) at H_{85}-CC and H_{85}-RN, and was even larger than K^* at H_7-CC where interpolated wind speeds were on average 1.5 m s^{-1} higher than at H_{85}-CC, thereby decreasing the value of the aerodynamic resistance to turbulent transfer. The highest daily contribution of Q_H at H_7-CC was 14 MJ on 2-May, when the interpolated wind speed (confirmed by W-AWS data) remained above 5 m s^{-1} for a period of 7 h, and air temperature reached a maximum of +15 °C (daily average 7.6 °C). In another MPB study of melt energetics, Boon (2007) simulated a higher mean contribution (74%) of net radiation to Q_M, but the clearcut was far smaller than the representative Baker clearcuts, with a mean wind speed of 0.5 m s^{-1} that was 70–80% lower than the mean wind speeds measured in this study (Table 6). Sensible heat flux has also shown to be the dominant energy source for melting in other clearcut areas, during certain meteorological conditions and periods of time (e.g., Koiuvusalo and Kokkenen, 2002).

Table 6
Mean meteorological characteristics for each accumulation and ablation season.

	2008				2009			
	Accumulation		Ablation		Accumulation		Ablation	
	W	Cen	*W*	Cen	*W*	Cen	*W*	Cen
T_A (°C)	−6.1	−6.7	0.4	1.9	−6.5	−7.6	1.9	3.5
U (m/s)	1.8	1.1	2.2	1.4	2.3	1.2	2.6	1.3
RH (%)	77	76	65	65	74	75	59	62
$K_\downarrow$ (W m^{-2})	63	65	182	182	66	65	204	204
$L_\downarrow$ (W m^{-2})	247	254	271	279	239	247	267	276
P (mm)	251	175	60	57	259	215	50	45

Latent heat flux Q_E represented a relatively small loss of energy at all stands, but was again proportionally higher across H_7 due to the enhanced wind speeds. The final sums of melt energy (Q_M) generally decreased with class PAI value, with ratios of Q_M in the dead mature GY stands representing 49 and 42% of the corresponding CC sums at H_{85} and H_7 respectively.

6.2. Catchment-scale simulations: current (MPB) landscape

Fig. 7 compares the simulated SWE across the catchment using the 2008 (MPB) land cover, with the available ground and MODIS measurements of snow-covered area (SCA) for three selected dates during snowmelt (see online version for colour format). Additionally shown are the catchment simulations of SWE distribution on 1-April of each year (i.e., within a few days of actual peak SWE occurrence), although no reliable MODIS imagery was available around this time to verify the catchment-wide snowcover that was simulated except for a few individual pixels located adjacent to the outlet. In terms of modelled SWE, there is a clear difference in elevational gradient between the 2 years, with a steeper gradient on 1-April 2008 resulting from less accumulated snow in the catchment interior and towards the outlet (i.e., <1000 m a.s.l.), but with similar accumulations in both years towards the highest elevations. Mean pixel SWE on 1-April 2008 was 127 mm, 22% lower than on 1-April 2009, but the pixel standard deviation of 37 mm was 6 mm higher than on 1-April 2009.

The meteorological conditions responsible for these gradient differences are revealed in Table 6, which summarises the mean AWS data from the W- and Cen-AWS sites representing the highest and lowest catchment AWS respectively. Mean conditions during snow accumulation (November–March) at W-AWS were slightly cooler (by 0.4 °C) and windier (by 0.5 m/s) in 2009 than 2008, although mean values of *RH*, $K_\downarrow$, $L_\downarrow$, and *P* were similar. More discernible changes occurred within the catchment interior at Cen-AWS, particularly in terms of temperature (0.9 °C cooler in 2009) and precipitation amount (23% higher) that at one point led measured mid-winter snowdepths to become equal to W-AWS snowdepths (2-February, Fig. 3), indicating a lower mean snowline for storm events in 2009. The peak SWE landscape survey data in Fig. 5 also support the diminished SWE gradient simulated in 2009, with SWE values for a given stand type decreasing in range between 2008 (e.g., 136 mm difference between the H_{85} and H_7 clearcut) and 2009 (31 mm difference). These important spatial changes in the meteorology and snow would not have been measured and simulated between years, if data were only available from one AWS or snow survey location with which to extrapolate across the catchment, as is a common method in many forest studies (e.g., B.C. Forest Practices Board, 2007),

During melt, the approximate snowline indicated by the MODIS data on 22-April 2008 was around 1000 m a.s.l., and the five

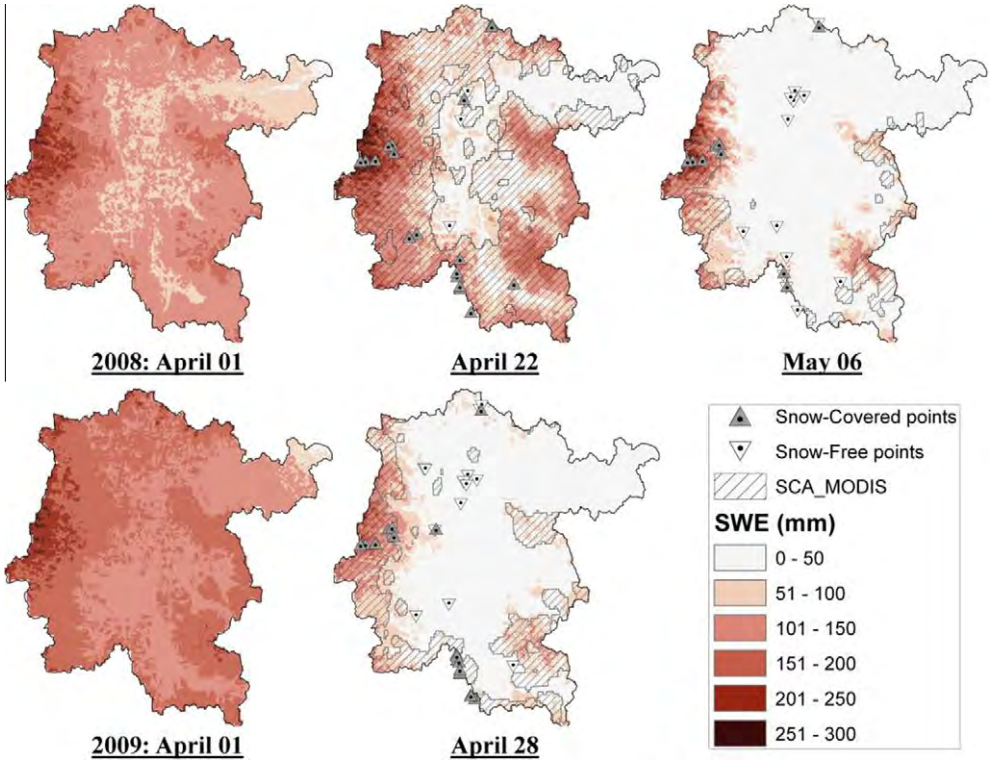

Fig. 7. Comparison of spatial snow distributions, including simulated SWE and MODIS or ground-based measurements of SCA.

measured snow-free sites on this date (Cen- and S-AWS, and H_{85}-CC, RN and GY) support this data. The SCA was generally well simulated by DHSVM, although the MODIS data suggest that an area between 950 and 1050 m a.s.l. in the east was actually snow-covered when much of it was simulated bare within the model, but no ground measurements were obtained here to verify this. In this instance, the extrapolation of weather data between eight distant AWS may still be insufficient to capture any synoptic gradients in the meteorological forcing, but two complete years of reliable air temperature data at similar elevation AWS suggest these gradients may be limited (monthly T_A values were on average 0.3 °C different between both W- and SE-AWS 29 km apart, and N- and SW-AWS 38 km apart.

Elsewhere, modelled SWE at the highest elevations increased slightly between 1 and 22 April (e.g., 14 mm at site H_7-CC), although measurements previously discussed for site H_7-CC decreased over the same period suggesting that the high-elevation snowfall events of 8- and 11-April were not melted sufficiently fast enough within the model. Mean catchment SWE on this date was 85 mm. On 6-May (mean SWE value 27 mm), the majority of remaining SWE identified by both measurements and MODIS data was at the highest elevations in the west, including all H_7, EB and W-AWS sites. Marginal snow conditions were indicated by the presence of both snow-covered and snow-free sites at H_{47} (northern boundary) and H_{27} (southern boundary), areas which were not snow-covered within the MODIS data but this could be due to the larger MODIS pixel size or errors within MODIS data at low snow-depths discussed previously. On 28-April 2009, SCA was accurately simulated by the model, including higher elevation sections (>1200 m a.s.l.) in the northeast and southeast, and almost the entire length of western and southern catchment boundary. The reason for this improved model performance in 2009 may be related to the more rapid ablation conditions and lack of snowfall events relative to 2008, which contribute substantially to model uncertainty as was shown at the stand-level for sites such as H_7-CC.

In terms of spatial snowmelt synchronisation, Fig. 8 displays the pixel mean snow accumulation and melt for both years, and indicates that simulated rapid ablation began around 4-April in both years, but thereafter ablation was more synchronised in 2009 than 2008, with the higher average snowpack melting out over a shorter period of 9 days, and the calculated mean ablation rate was 35% higher. Recorded temperatures from 1-April to 15-May were on average ~1.5 °C warmer in 2009 (Table 6), and only one spring snowfall event exceeding 10 mm water equivalent occurred after 4-April in 2009 (on 19-May, when the catchment was snow-free), whereas three occurred in 2008 (11- and 30-April, and 8-May) that raised snow albedo and extended the snowcover period especially at higher elevations. Clearcut snow survey or AWS measurements from both years support this trend, with elevations between H_{89} (Cen-AWS) and H_{28} (W-AWS) becoming snow free over an 11-day period (20-April to 1-May) in 2009, extending to a 29-day period (15-April to 14-May) in 2008. Additional LOCUS-3 data from plot H_7-CC in 2009 (but not 2008) suggest that most clearcuts in the catchment (range H_{89}–H_7) became snow free over the 20-day period between 20-April and 10-May 2009.

6.3. Catchment-scale simulations: MPB landscape changes

Between 2000 (pre-MPB) and 2008 (MPB), peak SWE values for April were simulated to increase by 12% using the 2008 meteorology, and by 19% using the 2009 meteorology, and corresponding melt rates increased by 10% and 15% (Fig. 8). Peak SWE increased more for the MPB landscape using the 2009 meteorology due to the calibration process used, which led almost all clearcut snow accumulation to be present in GY stands (98%, Table 3), whereas the corresponding values was lower in 2008 (84%, Table 3). The SWE ratio between healthy mature (GN) stands in the pre-MPB landscape, to clearcut values could only be estimated (75%) following measurements in other healthy stands (Spittlehouse, 2006), and this value was constant for either year. The simulated length

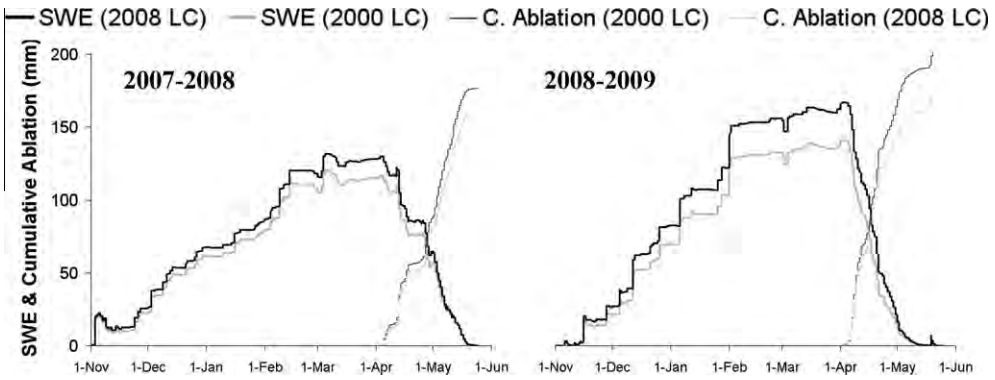

Fig. 8. Catchment snow trends, including pixel-mean values of SWE and cumulative ablation in 2008 and 2009, using the 2000 (pre-MPB) and MPB land covers (LC).

of melt period for either year was within 1-day between the two landscapes, but snow in the GN stands as part of the 2000 landscape may have melted too quickly in the model by using albedo decay parameters that were parameterised for the GY stands, of potentially higher litter concentrations than for GN stands.

On an earlier draft of this manuscript, one anonymous referee made the comment that the above percentages suggest that MPB may not have as big of an effect on the snow hydrology as one might expect. We argue that the relation between MPB and snow hydrology cannot be revealed without invoking the effects of melt water input to soil on runoff delivery to channels, likely to be synchronized and hence amplified by the subdued topography typical of our study watershed. In addition, although it may be obvious that the combination of greater accumulation of snow and energy inputs to snow in a disturbed watershed will cause greater rates of water input to soil, "we need to know how often this situation occurs" (Berris and Harr, 1987, p. 141). Our predicted increase in snow accumulation and ablation rates during the period of MPB changes, together with the reduction of transpiration, is likely to increase the soil moisture storage, water available for local and downstream runoff and ultimately the magnitude and frequency of annual stream discharge events. Traditional forest hydrology studies seeking to quantify the effects of forest land-use changes on the magnitude of peak flows used analysis of variance and covariance of chronologically-paired control and treatment events (comparing peak discharge events of the same storm or meteorological input) as part of a paired-watershed experimental design, but this method leads to incorrect estimate of changes in event magnitude because it does not account for the consequential changes in event frequency (Alila et al., 2009). Analysis employing a frequency-pairing approach (comparing peak discharge events occurring with the same probability of occurrence) suggests that even small changes in the magnitude, such as the small increases in water input estimated from this study (10–20%), may translate to disproportionately large changes in the corresponding frequencies resulting from the non-linearity in the relation between the magnitude of peak flow events and their frequencies (Alila et al., 2009). The occurrence of more frequent same-magnitude runoff events, or higher magnitude events of same frequency, are likely to be amplified in watersheds with milder slope flood frequency curves (Harr, 1981; Berris and Harr, 1987; Alila et al., 2009), typical of snow dominated regimes. These more frequent higher magnitude events, of potentially increased flashiness due to synchronisation of water delivery in subdued topography, may have negative impacts on channel morphology, water quality and aquatic ecosystems, in addition to the important social consequences such as localized flooding of agricultural land and road degradation that has already increased in frequency at Baker Creek during MPB.

7. Conclusions

In this study, the forest disturbance due to Mountain Pine Beetle infestation on snow accumulation and ablation has been studied using a combination of extensive measurements and the DHSVM model. The model was calibrated for the Baker Creek catchment to improve most notably the accuracy of simulated peak SWE differences between representative MPB stands, the important changes in solar radiation transmission as a function of canopy structure and time of year, and solar reflection as a function (primarily) of litterfall relating to infestation stage. With all healthy mature pine stands that dominated the catchment up until 2000 having been killed by MPB or been subsequently logged, a combination of these measurements and model simulations indicated that snow accumulation and ablation rates were more synchronised between stands in the current (MPB) landscape than in 2000, but literature-based values had to be applied to parameterise the healthy pine stand characteristics. Measured peak SWE values imply that that during snow accumulation, any snow interception by dead mature stands appears to be almost completely offset by the enhanced rates of clearcut sublimation and any melting, and even blowing snow erosion that may now occur in larger clearcuts representative of MPB catchments. Similarly, most regenerating stands in the catchment are of insufficient canopy density (through young age or MPB infestation) to change peak SWE values much beyond the clearcut or dead mature stand values. Uncertainties in the model algorithms simulating these processes were essentially masked by fine-tuning snowfall estimates until the simulated peak SWE values matched clearcut measurements at each AWS, and subcanopy peak SWE values were calibrated to match the mean ratios of subcanopy to clearcut SWE measured across the catchment for each major stand type. Additional work will be required to improve not only the model algorithms describing the mass and energy transfers such as canopy interception, blowing snow transport, and increased efficiency of longwave emissions, but also the model initialisation data (e.g., stand specific canopy values from remotely-sensed data). The strength of these stand relationships should also be tested within a much lower snowpack year, when variations in snow accumulation are likely to be enhanced.

At the catchment scale, model simulations of snowmelt and snow-covered area for the 2008 and 2009 winter periods compared relatively well to distributed satellite or ground-based measurements, with more synchronised melting in 2009 resulting from a more homogenous (elevation-independent) peak SWE distribution, warmer temperatures and absence of snowfall events during the spring. Simulations across the pre-MPB landscape in 2000 using the same input meteorological data indicated a 10–20% increase in both catchment snow accumulation and melt rates over

the 8-year period of MPB effects, resulting in almost no difference in period of snowcover. A greater snowpack volume, which enters the stream network faster, inevitably has implications for stream runoff characteristics, flood risks and water resources, and this is already apparent in the form of unprecedented spring flooding that has occurred annually in parts of Baker Creek since MPB began. The next stage of this research study is to quantify the MPB change to stream runoff characteristics across Baker, by integrating the snowmelt distributions resulting from this study within a transient, three-dimensional representation of surface and saturated subsurface flow (Wigmosta et al., 2002). These simulations will also be extended further in time to incorporate the effects that may occur due to future predicted rates of salvage logging and plant regeneration within the catchment.

Acknowledgements

This research was supported by the National Science and Engineering Research Council of Canada, British Columbia Ministry of the Environment, Forest Practices Board of British Columbia, and Natural Resources Canada (Mountain Pine Beetle Initiative). We acknowledge Environment Canada agency and staff for long-term monitoring and for making data available to the wider science community. The authors would also like to thank Piotr Kuraś, Dennis Gordon, Pat Teti, Tim Blair, Philip Marren and Patrick Little for their help with the snow surveys, Nicholas Coops and Chris Bater for their assistance in obtaining the Landsat data and Jens Wawerla for processing LOCUS-3 data. Rita Winkler, Dave Spittlehouse and Dan Moore provided invaluable comments on an initial draft of this paper, and Georg Jost provided the necessary help to begin running DHSVM version 3. The comments from five anonymous reviewers were also critical in improving the clarity and structure of this paper.

References

Alila, Y., Kuras, P.K., Schnorbus, M., Hudson, R., 2009. Forests and floods: a new paradigm sheds light on age-old controversies. Water Resour. Res. 45, W08416. doi:10.1029/2008WR007207.

Anderson, E.A., 1976. A Point Energy and Mass Balance Model of a Snow Cover. NOAA Technical Report NWS 19, 150 pp.

Ault, T., Czajkowski, K.P., Benko, T., Coss, J., Struble, J., Spongberg, A., Templin, M., Gross, C., 2006. Validation of the MODIS snow product and cloud mask using student and NWS cooperative station observations in the lower great lakes region. Remote Sens. Environ. 105, 341–353.

B.C. Forest Practices Board, 2007. The Effect of Mountain Pine Beetle Attack and Salvage Harvesting on Streamflows. FPB/SIR/16, Victoria, BC.

B.C. Ministry of Environment. 2009. Snowpack and Water Supply Outlook for British Columbia. April 1 snow survey bulletin (<http://ww.env.gov.bc.ca/rfc/archive/2006/200604/bulletin.htm>).

B.C. Ministry of Forests. 2004. MPB Salvage – Hydrology Recommendations (<http://www.for.gov.bc.ca/hfp/mountain_pine_beetle/stewardship/Hydrological%20Recommendations%20Dec%203%202004.pdf>).

Berris, S.N., Harr, R.D., 1987. Comparative snow accumulation and melt during rainfall in forested and clear-cut plots in the Western Cascades of Oregon. Water Resour. Res. 23 (1), 135–142.

Bethlahmy, N., 1975. A Colorado episode: beetle epidemic, ghost forests, more streamflow. Northwest Sci. 49, 95–105.

Boon, S., 2009. Snow ablation energy balance in a dead forest stand. Hydrol. Proc. 23, 2600–2610.

Boon, S., 2007. Snow accumulation and ablation in a beetle-killed pine stand, northern Interior British Columbia, BC. J. Ecosyst. Manage. 8, 1–13.

Bowling, L.C., Storck, P., Lettenmaier, D.P., 2000. Hydrologic effects of logging in Western Washington, United States. Water Resour. Res. 36, 3223–3240.

Brazenec, W.A., 2005. Evaluation of Ultrasonic Snow Depth Sensors for Automated Surface Observing Systems (ASOS). Department of Forest, Rangeland, and Watershed Stewardship, M.S. Thesis, Colorado State University, Fort Collins, CO, 134 pp.

Essery, R., Pomeroy, J.W., 2004. Vegetation and topographic control of wind-blown snow distributions in distributed and aggregated simulations for an arctic tundra basin. J. Hydrometeorol. 5, 735–744. Special Section.

Hall, D.K., Riggs, G.A., Salomonson, V.V., 2000. MODIS/Terra Snow Cover Daily L3 Global 500m Grid V005, March 2008–May 2008. National Snow and Ice Data Center. Digital Media. Boulder, CO, USA. 2000. updated daily.

Hall, D.K., Riggs, G.A., 2007. Accuracy assessment of the MODIS snow-cover products. Hydrol. Proc. 21, 1534–1547.

Hedstrom, N.R., Pomeroy, J.W., 1998. Measurements and modelling of snow interception in the boreal forest. Hydrol. Proc. 12, 1611–1625.

Hendrick, R., Filgate, B., Adams, W.M., 1971. Application of environmental analysis to watershed snowmelt. J. Appl. Metal. 10, 418–429.

Harr, R.D., 1981. Some characteristics and consequences of snowmelt during rainfall in western Oregon. J. Hydrol. 53, 277–304.

Jackson, S.I., Prowse, T.D., 2009. Spatial variations of snowmelt and sublimation in a high-elevation semi-desert basin of western Canada. Hydrol. Proc. 18, 2611–2627.

Jost, G., Moore, R.D., Weiler, M., Gluns, D., Alila, Y., 2009. Use of distributed snow measurements to test and improve a snowmelt model for predicting the effect of forest clear-cutting. J. Hydrol. 376, 94–106.

Koivusalo, H., Kokkonen, T., 2002. Snow processes in a forest clearing and in a coniferous forest. J. Hydrol. 262, 145–164.

Koivusalo, H., Kokkonen, T., Laurén, A., Ahtiainen, M., Karvonen, T., Mannerkoski, H., Penttinen, S., Seuna, P., Starr, M., Finér, L., 2006. Parameterisation and application of a hillslope hydrological model to assess impacts of a forest clear-cutting on runoff generation. Environ. Modell. Softw. 21, 1324–1339.

Ladekarl, U.L., Norberg, P., Rasmussen, K.R., Nielsen, K.E., Hansen, B., 2001. Effects of heather beetle attack on soil moisture and water balance at a Danish heathland. Plant Soil 229, 147–158.

Lamarche, J., Lettenmaier, D.P., 1998. Effects of forest roads on flood flows in the Deschutes river basin, Washington. Earth surf. Process. Landforms 26, 115–134.

Lanini, J.S., Clark, E.A., Lettenmaier, D.P., 2009. Effects of fire-precipitation timing and regime on post-fire sediment delivery in Pacific Northwest forests. Geophys. Res. Lett. 36, L01402. doi:10.1029/2008GL034588.

Liston, G.E., Elder, K., 2006. A meteorological distribution system for high-resolution terrestrial modeling (MicroMet). J. Hydrometeorol. 7, 217–234.

Lord, T.M., Mackintosh, E.E., 1982. Soil inventory report: Soils of the Quesnel Area, British Columbia. British Columbia Soil Survey Report No. 31, Research Branch, Agriculture Canada, Ottawa, Ontario, 45 pp.

Love, L.D., 1955. The effect on streamflow of the killing of spruce and pine by the Engelmann spruce beetle. Trans. Am. Geophysical. Union 36, 113–118.

Lundquist, J., Cayan, D., Dettinger, M., 2004. Spring onset in the Sierra Nevada: When is snowmelt independent of elevation? J. Hydrometeorol. 5, 325–340.

Marks, D., Winstral, A., Seyfried, M., 2002. Investigation of terrain and forest shelter effects on patterns of snow deposition, snowmelt and runoff over a semi-arid mountain catchment using simulated snow redistribution fields. Hydrol. Proc. 16, 3605–3626.

Mitchell, R.G., Preisler, H.K., 1998. Fall rate of lodgepole pine killed by the mountain pine beetle in central Oregon. West. J. Appl. Forest 13, 23–26.

Monteith, J., Unsworth, M., 1990. Principles of Environmental Physics, London, Edward Arnold.

Neumann, N.N., Derksen, C., Smith, C., Goodison, B., 2006. Characterizing local scale snow cover using point measurement during the winter season. Atmos. Ocean 44, 257–269.

Nijssen, B., Lettenmaier, D.P., 1999. A simplified approach for predicting shortwave radiation transfer through boreal forest canopies. J. Geophys. Res. 104, 27859–27868.

Pomeroy, J.W., Marks, D., Link, T., Ellis, C., Hardy, J., Rowlands, A., Granger, R., 2009. The impact of coniferous forest temperature on incoming longwave radiation to melting snow. Hydrol. Proc. 23, 2513–2525. doi:10.1002/hyp. 7325.

Pomeroy, J.W., Li, L., 2000. Prairie and Arctic areal snow cover mass balance using a blowing snow model. J. Geophys. Res. 105 (D21), 26619–26634.

Pomeroy, J.W., Gray, D.M., Shook, K.R., Toth, B., Essery, R.L.H., Pietroniro, A., Hedström, N., 1998. An evaluation of snow accumulation and ablation processes for land surface modelling. Hydrol. Proc. 12, 2339–2367.

Pomeroy, J.W., Dion, K., 1996. Winter radiation extinction and reflection in a boreal pine canopy: measurements and modelling. Hydrol. Proc. 10, 1591–1608.

Potts, D.F., 1984. Hydrologic impacts of a large-scale mountain pine beetle (*Dendroctonus ponderosae* Hopkins) epidemic. Water Resour. Bull. 20, 373–377.

Sicart, J.E., Pomeroy, J.W., Essery, R.L.H., Hardy, J., Link, T., Marks, D., 2004. A sensitivity study of daytime net radiation during snowmelt to forest canopy and atmospheric conditions. J. Hydrometeorol. 5, 774–784.

Spittlehouse, D.L., 2006. Annual water balance of high elevation forests and clearcuts. In: Proceedings of the 27th Conference on Agricultural and Forest Meteorology, San Diego, CA, American Meteorological Society, Boston, MA, 7 pp.

Storck, P., 2000. Trees, snow and flooding. An investigation of forest canopy effects on snow accumulation and melt at the plot and watershed scales in the Pacific Northwest. In: Water Resources Series, Technical Report 161. University of Washington, Seattle, WA, 176 pp.

Storck, P., Lettenmaier, D.P., 1999. Predicting the effect of a forest canopy on ground snow pack accumulation and ablation in maritime climates. In: Proceedings of the 67th Western Snow Conference, South Lake Tahoe, California, pp. 1–12.

Summit Environmental Consultants Ltd., 2007. Baker Creek Watershed Assessement-Phases 1 & 2, Vernon, BC, 175 pp.

Suzuki, K., Kubota, J., Zhang, Y.S., Kadota, T., Ohata, T., Vuglinsky, V., 2006. Snow ablation in an open field and larch forest of the southern mountainous region of eastern Siberia. Hydrol. Sci. J. 51, 465–480.

Tabler, R. D., 1973. Evaporation losses of windblown snow, and the potential for recovery. In: Proceedings of the 41st Western Snow Conference, Grand Junction, CO, April 17–19 1973, pp. 75–79.

Teti, P., Winkler, R., 2008. Snow hydrology and solar radiation in growing and deteriorating pine stands, BC. J. Ecosyst. Manage. 9, 136–138.

Thyer, M., Beckers, J., Spittlehouse, D., Alila, Y., Winkler, R., 2004. Diagnosing a distributed hydrologic model for two high-elevation forested catchments based on detailed stand- and basin-scale data. Water Resour. Res. 40, W01103. doi:10.1029/2003WR002414.

Whitaker, A., Alila, Y., Beckers, J., Toews, D., 2003. Application of the Distributed Hydrological Soil Vegetation Model to Redfish Creek, British Columbia: Model evaluation using internal catchment data. Hydrol. Proc. 17, 199–224.

Wigmosta, M.S., Nijssen, B., Storck, P., Lettenmaier, D.P., 2002. The distributed hydrology soil vegetation model. In: Singh, V.P., Frevert, D.K. (Eds.), Mathematical Models of Small Watershed Hydrology and Applications, Water Resource Publications, Littleton, CO, pp. 7–42.

Winkler, R., Boon, S., 2009. A Summary of Research into the Effects of Mountain Pine Beetle Related Stand Mortality on Snow Accumulation and Ablation in BC. In: Proceedings of the 77th Annual Western Snow Conference, Canmore, AB, 20–24 April.

Winkler, R., Spittlehouse, D.L., Golding, D.L., 2005. Measured differences in snow accumulation and melt among clearcut, juvenile, and mature forests in southern British Columbia. Hydrol. Proc. 19, 51–62.